

Inversion of Stokes Profiles with Systematic Effects

A. Asensio Ramos^{1,2}, J. de la Cruz Rodríguez³, M. J. Martínez González^{1,2}, and A. Pastor Yabar^{1,2}

¹ Instituto de Astrofísica de Canarias, 38205, La Laguna, Tenerife, Spain; e-mail: aasensio@iac.es

² Departamento de Astrofísica, Universidad de La Laguna, E-38205 La Laguna, Tenerife, Spain

³ Institute for Solar Physics, Dept. of Astronomy, Stockholm University, Albanova University Center, 10691 Stockholm, Sweden
e-mail: jaime@astro.su.se

Received —; accepted —

ABSTRACT

Quantitative thermodynamical, dynamical and magnetic properties of the solar and stellar plasmas are obtained by interpreting their emergent non-polarized and polarized spectrum. This inference requires the selection of a set of spectral lines particularly sensitive to the physical conditions in the plasma and a suitable parametric model of the solar/stellar atmosphere. Nonlinear inversion codes are then used to fit the model to the observations. However, the presence of systematic effects like nearby or blended spectral lines, telluric absorption or incorrect correction of the continuum, among others, can strongly affect the results. We present an extension to current inversion codes that can deal with these effects in a transparent way. The resulting algorithm is very simple and can be applied to any existing inversion code with the addition of a few lines of code as an extra step in each iteration.

Key words. Sun: magnetic fields, atmosphere — line: profiles — methods: data analysis

1. Introduction

The decade of 1970's will be remembered as the one in which Solar Physicist were able to really start to infer the magnetic and thermodynamic properties of the solar plasma from the observations. At that specific time, there was a sweet coincidence. On the one hand, the theory of radiative transfer for polarized light was already in its maturity. On the other, computers started to be available for researchers in general and powerful enough to carry out complex calculations. It was then the time at which the ideas of non-linear inversion codes were set (Harvey et al. 1972; Auer et al. 1977; Skumanich & Lites 1987).

Inversion algorithms are able to extract information about the magnetic and thermodynamical properties of the solar plasma from the analysis of spectropolarimetric observations. They function by proposing a specific model to explain the observations and then defining a merit function (usually the χ^2 function, valid under the presence of uncorrelated Gaussian noise). The model parameters are iteratively modified for optimizing the merit function. The first inversion codes were relatively simple and based on strongly simplifying assumptions, like the Milne-Eddington (ME) approximation to analytically solve the radiative transfer equation (e.g., Harvey et al. 1972; Auer et al. 1977; Landi Degl'Innocenti & Landolfi 2004). Such inversion codes are still used today, like VFISV (Borrero et al. 2007, 2010), MILOS (Orozco Suárez et al. 2007) or MERLIN (Skumanich & Lites 1987; Lites et al. 2007).

An enormous step forward was introduced by Ruiz Cobo & del Toro Iniesta (1992), who developed SIR (Stokes Inversion based on Response functions), an inversion code that recovers the optical depth stratification of the physical quantities (temperature, magnetic field, velocity, etc.) from the interpretation of the Stokes profiles. These codes are based on the idea of response function (Landi Degl'Innocenti & Landi Degl'Innocenti 1977), that allows the user to link the perturbation in the emergent Stokes parameters with perturbations in the physical pa-

rameters. One of the key ingredients that facilitated the development of such inversion codes was the possibility to find an analytical expression for the response functions in local thermodynamic equilibrium (LTE) (Sanchez Almeida 1992; Ruiz Cobo & del Toro Iniesta 1994). Based on the seed of SIR, several non-linear inversion codes are now available, some of them even dealing with the much more difficult case of the inversion of spectral lines in non-LTE (NICOLE; Socas-Navarro et al. 2000, 2014). All these 1D inversion codes are based on the concept of “nodes”, that need to be defined a-priori. These nodes mark positions along the optical depth axis where the value of the physical parameters will be modified to fit the Stokes profiles. The full stratification of the atmosphere between the nodes, which is needed to accurately integrate the radiative transfer equation and to derive the gas pressure scale, is interpolated using a piecewise polynomial. The complexity of the solution then critically depends on the number of nodes that are employed to describe each of the physical parameters.

After more than a decade without any fundamental improvement (except perhaps the introduction of Bayesian inference into the field; Asensio Ramos et al. 2007; Asensio Ramos 2009; Asensio Ramos et al. 2012), we are nowadays living another sweet era, again driven by the improvements in computational power. On one side, van Noort (2012) has developed a spatially coupled two-dimensional inversion code in which the effect of the telescope point spread function (PSF) is taken into account. The PSF couples nearby pixels so that deconvolution and inversion is done at the same time. Following a similar motivation, Ruiz Cobo & Asensio Ramos (2013) have used a regularized deconvolution of the Stokes profiles based on the principal component analysis (PCA) and have used SIR to invert the deconvolved Stokes parameters.

Arguably, the last step in the evolution of inversion codes has been the introduction of regularization ideas based on the

arXiv:1604.05470v1 [astro-ph.SR] 19 Apr 2016

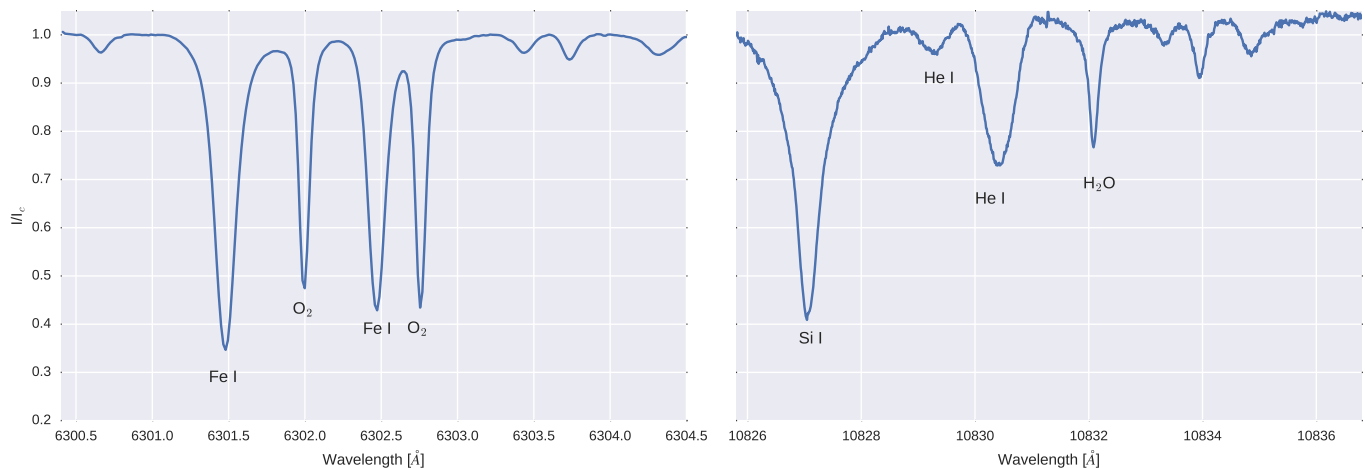


Fig. 1. Examples of situations in which systematic effects are important when extracting information from spectral lines.

concept of sparsity or compressibility¹ (e.g., Starck et al. 2010). Asensio Ramos & de la Cruz Rodríguez (2015) have presented an inversion code for the inversion of Stokes profiles that uses ℓ_0 or ℓ_1 regularization on a transformed space². The two-dimensional maps of parameters are linearly transformed (Fourier, wavelet or any other appropriate transformation can be used) and assumed to be sparse in the transformed domain. This introduces two important constraints. First, the sparsity assumption reduces the number of unknowns in the problem, avoiding overfitting. Second, the global character of the transformations that are routinely used, spatial correlation of the result is automatically taken into account. Consequently, the Stokes parameters observed at every pixel potentially introduces constraints onto every other pixel of the observed map. This is the first time that the inherent spatial correlation of the physical parameters has been taken into account in inversion codes. This results into much more stable inversion codes that do not produce spurious pixel-by-pixel variations of the maps of physical quantities. Additionally, the complexity of the solution is automatically adapted, producing more structure where it is needed.

In the conclusions of Asensio Ramos & de la Cruz Rodríguez (2015) we pointed out that the sparsity regularization can be applied to invert Stokes profiles with systematic effects. This is precisely what we present in this paper. A customary way of dealing with systematic effects in current inversions is to down-weight the influence on the merit function of the parts of the spectrum that are affected by these effects. Although it works in practice, it depends on a set of parameters (e.g., region and factor of the downweighting) that make it quite subjective. Instead, we propose several basis sets (orthogonal and non-orthogonal) to absorb the systematic effects (for instance, telluric lines) in the Stokes profiles and use a proximal projection algorithm (e.g., Parikh & Boyd 2014) to make the solution automatically adapt to the necessary complexity. We will show that the modifications needed in existing inversion codes are minimal so that this approach can be introduced without much effort.

¹ Given an n -dimensional vector \mathbf{x} , sparsity means that the majority of the elements of the vector are strictly zero, while compressibility means that the elements of such vector, when ordered by absolute value, fulfill $|x_i| \leq Ci^{-1/r}$.

² The ℓ_p -norm is given by: $\|\mathbf{x}\|_p = (\sum_i |x_i|^p)^{1/p}$, with $p \geq 0$.

2. Sparsity regularization

Our objective is to fit the observed Stokes parameters, that are discretized at N finite wavelength points λ_j . For simplicity, we stack the four Stokes parameters in a long vector of length $4N$ so that $\mathbf{O} = [I(\lambda_1), \dots, I(\lambda_N), Q(\lambda_1), \dots, U(\lambda_1), \dots, V(\lambda_1), \dots, V(\lambda_N)]^\dagger$ (with \dagger the transpose). The fit is carried out using a model atmosphere, with the aim of extracting useful thermal, dynamic and magnetic information from them. Additionally, we make the assumption that these Stokes parameters are perturbed by some uncontrollable systematic effects. These systematic effects can be, for instance, telluric lines produced by absorption in the Earth atmosphere, variations along the spectral direction produced by an incorrect illumination of the camera or a low-quality flatfielding, etc. Examples of these situations are found in Fig. 1. The left panel shows the well-known region around 6302 Å that contains two Fe I lines, which are blended with two telluric lines. This is of special importance for the Fe I line at 6302.5 Å. Extracting physical information from the line requires then to avoid the far wings, which can lead to problems in the deepest parts of the atmosphere. The right panel shows the region around 10830 Å, containing a He I multiplet used for chromospheric diagnostics, which is blended with a photospheric Si I line and a telluric line. The interpretation of the He I multiplet, given that it forms on the extended wings of the Si I line, usually requires a previous analysis of the photospheric line. Additionally, the strong chromospheric dynamics induces that the He I multiplet sometimes blends with the telluric absorption.

In very general terms, we can explain the observations with the following generative model:

$$\mathbf{O} = \mathbf{S}_{\text{atm}}(\mathbf{q}) + \mathbf{D}\boldsymbol{\alpha} + \boldsymbol{\epsilon}, \quad (1)$$

where $\boldsymbol{\alpha}$ is a vector of dimension d that describes the systematic effects via a dictionary $\mathbf{D} \in \mathbb{R}^{4N \times d}$, also known as synthesis operator. We remind that a dictionary is just a collection of (possibly non-orthogonal) functions that are used to describe the systematic effects. The contribution $\mathbf{S}_{\text{atm}}(\mathbf{q})$ contains the Stokes parameters that emerge from a model atmosphere depending on a vector of model parameters \mathbf{q} , ordered like in \mathbf{O} . The noise components $\boldsymbol{\epsilon}$ are considered to be Gaussian random variables with zero mean and diagonal covariance matrix. Note that when

the size of the dictionary equals the number of observed spectral points ($d = 4N$) and $\mathbf{D} = \mathbf{1}$ (with $\mathbf{1}$ the identity matrix), the model for the systematic effects described in Eq. (1) turns out to be very flexible because α refers to the particular value of the systematic effects at each sampled wavelength point.

From this generative model, the merit function one has to optimize is the χ^2 with diagonal covariance, in our case given by:

$$\chi_{\mathbf{D}}^2(\mathbf{q}, \alpha) = \frac{1}{4N} \sum_{j=1}^{4N} w_j \frac{[S_{\text{atm},j}(\mathbf{q}) + (\mathbf{D}\alpha)_j - O_j]^2}{\sigma_j^2}, \quad (2)$$

where we make explicit the dependence of the merit function on the election of the dictionary. The previous merit function considers a potentially different noise variance σ_j^2 for every Stokes parameter and wavelength position, which is surely the case for very strong lines in which the number of photons in the core is much more absorbed than the wings. Additionally, it is customary to introduce weights w_j for each Stokes parameter to increase the sensitivity to some parameters when carrying out the inversion³. These weights are precisely the ones that are currently used to deal with systematic effects, by decreasing their values for specific wavelength points.

The inferred physical parameters are typically found by solving the following maximum-likelihood problem:

$$\underset{\mathbf{q}, \alpha}{\operatorname{argmin}} \chi_{\mathbf{D}}^2(\mathbf{q}, \alpha), \quad (3)$$

where the operator “argmin” returns the value of \mathbf{q} and α that minimizes the $\chi_{\mathbf{D}}^2(\mathbf{q}, \alpha)$ function. Note that Eq. (3) is, in general, non-convex⁴ for the inversion of Stokes parameters. Therefore, we only aspire to reach one of the local minima and later check for the physical relevance of the solution. Problem (3) is usually solved by direct application of the Levenberg-Marquardt (LM) algorithm (Levenberg 1944; Marquardt 1963), which is especially suited to the optimization of such ℓ_2 -norms. Although problem (3) is stated without any constraint, it is clear from the introduction that it is customary to regularize the solution by imposing some regularity of the solution through the use of nodes. Consequently, the vector of parameters \mathbf{q} contains the value of the physical parameters (temperature, magnetic field, velocity, ...) at a small number of depths in optical depth in the atmosphere. In between these points, the physical properties are interpolated from the values at these nodes.

Without any additional constraint for α , it is sure that we will encounter cross-talk between α and \mathbf{q} . The fundamental reason is that our regressor for the systematic effects is so flexible that it can potentially fit the observations perfectly, including the specific noise realization. As noted above, if $d = 4N$ and $\mathbf{D} = \mathbf{1}$, a solution to Eq. (3) is $\alpha = \mathbf{0}$ and $\mathbf{S}_{\text{atm}}(\mathbf{q}) = 0$ for every observed wavelength. This trivial solution is of no interest because it does not extract any relevant physical information from the observations. In order to overcome this possibility, we follow recent ideas (Candès et al. 2006; Starck et al. 2010; Asensio Ramos

& de la Cruz Rodríguez 2015) and regularize the problem by imposing a sparsity constraint on α or, in general, in any transformation of α . Two fundamental approaches to include this sparsity penalty have been proposed (Starck et al. 2010). Each one has advantages and disadvantages, as we will show in Sec. 4.

2.1. The analysis penalty approach

This approach is based on having as many degrees of freedom as observed data points ($d = 4N$) and $\mathbf{D} = \mathbf{1}$ and solving the following problem:

$$\underset{\mathbf{q}, \alpha}{\operatorname{argmin}} \chi_{\mathbf{1}}^2(\mathbf{q}, \alpha), \text{ subject to } \|\mathbf{W}\alpha\|_p \leq s, \quad (4)$$

where \mathbf{W} is the matrix associated to any linear transformation of interest, either orthogonal or not, while s is a predefined threshold. We also remind the reader that $\|\mathbf{x}\|_p = (\sum_i |x_i|^p)^{1/p}$ is the ℓ_q -norm. For instance, the ℓ_0 norm of a vector is just the number of non-zero elements, while the ℓ_1 norm is the sum of the absolute value of its elements. Put in words, solving Eq. (4) requires to seek the pair (\mathbf{q}, α) that better fits our observations, imposing that the projection of the systematic effects on the transformed domain defined by \mathbf{W} is sparse. The name *analysis penalty* comes from the fact that \mathbf{W} is the analysis operator, that carries the vector α to the transformed sparsity-inducing domain (Elad et al. 2007; Starck et al. 2010). It is especially suited to deal with cases in which \mathbf{W} is non-orthogonal and/or overcomplete.

The solution to the previous problem when $p = 0$ (or equivalently when $p = 1$ under some conditions; Candès et al. 2006; Donoho 2006) is known to coincide with the exact solution when it exists. Sparsity is, therefore, a very convenient regularization. The only degree of freedom is to find the appropriate transformation \mathbf{W} . The same problem can be equivalently written with the addition of a regularization parameter (λ):

$$\underset{\mathbf{q}, \alpha}{\operatorname{argmin}} \left[\frac{1}{4N} \sum_{j=1}^{4N} w_j \frac{[S_{\text{atm},j}(\mathbf{q}) + \alpha_j - O_j]^2}{\sigma_j^2} + \lambda \|\mathbf{W}\alpha\|_p \right]. \quad (5)$$

2.2. The synthesis penalty approach

This approach is based on having $\mathbf{D} = \mathbf{W}^T$, and imposing a sparsity constraint on the α vector itself. Consequently, we have to solve the problem

$$\underset{\mathbf{q}, \alpha}{\operatorname{argmin}} \chi_{\mathbf{W}^T}^2(\mathbf{q}, \alpha), \text{ subject to } \|\alpha\|_p \leq s, \quad (6)$$

which, in lagrangian form, becomes:

$$\underset{\mathbf{q}, \alpha}{\operatorname{argmin}} \left[\frac{1}{4N} \sum_{j=1}^{4N} w_j \frac{[S_{\text{atm},j}(\mathbf{q}) + (\mathbf{W}^T \alpha)_j - O_j]^2}{\sigma_j^2} + \lambda \|\alpha\|_p \right], \quad (7)$$

The name *synthesis penalty* comes from the fact that \mathbf{W}^T is the synthesis operator, that generates the systematic effects from the vector α living on the sparsity-inducing transformed domain.

It was noted by Elad et al. (2007) that both approaches are equivalent when \mathbf{W} is an orthogonal transform (like Fourier, wavelet, ...), because it fulfills $\mathbf{W}^T \mathbf{W} = \mathbf{1}$. However, they solve completely different problems when \mathbf{W} is non-orthogonal.

³ Note that the role of the weights is to modify the value of the noise variance. If the noise variance is artificially increased for one Stokes parameter, its constraining power decreases.

⁴ When the function to minimize is convex in the variables, a local minimum is also the global minimum. This cannot be guaranteed in the optimization of non-convex functions, which is typically the case in the inversion of Stokes parameters

2.3. Transformations

We will consider in this paper three options for the regularization term. The first one uses as regularization an orthogonal wavelet transform. The fact that \mathbf{W} is orthogonal will slightly simplify the algorithms. The second one is a non-orthogonal overcomplete isotropic undecimated wavelet transform using the B_3 -spline (Starck et al. 2010). Finally, we will use a hand-made non-orthogonal transform made of Voigt functions centered at specific locations in the spectrum, that will be used to absorb the systematic effects. We defer the detailed description of each one until Sec. 3.3.

3. The proposed optimization

Given the special structure of both problems defined in Eqs. (5) and (7), in which the regularization only occurs for the α variables, we propose to use an alternating optimization method. If α is fixed, Eq. (5) becomes the traditional least-squares problem for \mathbf{q} , that is solved efficiently with Newton-type methods like the Levenberg-Marquardt algorithm. This method uses second-order information given by \mathbf{H}_q , the Hessian of the merit function with respect to the \mathbf{q} variables:

$$\mathbf{q}_{i+1} = \mathbf{q}_i - \hat{\mathbf{H}}_q^{-1} \nabla_q \chi_1^2(\mathbf{q}_i, \alpha_i) \quad \text{with } \alpha_i \text{ fixed.} \quad (8)$$

Conforming to the prescriptions of the Levenberg-Marquardt algorithm, we use a modified Hessian matrix by enhancing its diagonal by a factor β , so that $\hat{\mathbf{H}}_q = \mathbf{H}_q + \beta \text{diag}(\mathbf{H}_q)$. This hyperparameter is modified during the iteration to shift between the gradient descent method (large β) and Newton-type method (small β). We note that inverting the Hessian matrix with a truncated singular value decomposition (Ruiz Cobo & del Toro Iniesta 1992) introduces an extra regularization on the physical parameters at the nodes that is often needed.

3.1. The analysis penalty

On the other hand, when \mathbf{q} is fixed, Eq. (5) becomes a standard sparsity-constrained linear problem for α . This problem can be solved efficiently using proximal algorithms (Parikh & Boyd 2014; Asensio Ramos & de la Cruz Rodríguez 2015), which are especially suited to solve problems of the type

$$\underset{\alpha}{\text{argmin}} f(\alpha) := g(\alpha) + h(\alpha), \quad (9)$$

where $g(\alpha) = \chi_1^2(\mathbf{q}, \alpha)$, is a smooth function and $h(\alpha) = \lambda \|\mathbf{W}\alpha\|_p$ is a convex but not necessarily smooth function (note that the derivative of the $\|\mathbf{W}\alpha\|_p$ term is not continuous). We propose the following first-order iterative scheme to solve the problem:

$$\alpha_{i+1} = \text{prox}_{p,\lambda,\mathbf{W}} \left[\alpha_i - \tau \nabla_{\alpha} \chi_1^2(\mathbf{q}_{i+1}, \alpha_i) \right] \quad \text{with } \mathbf{q}_{i+1} \text{ fixed,} \quad (10)$$

where the operator $\text{prox}_{p,\lambda,\mathbf{W}}$ is the proximal projection operator (Parikh & Boyd 2014) associated with the constraint $\|\mathbf{W}\alpha\|_p$, that we show how to efficiently compute in Sec. 4. The election of the step size τ is important for the convergence of the algorithm. It is known to converge provided the step size fulfills $\tau < 2/\|\mathbf{H}_\alpha\|^2$, where $\|\mathbf{H}_\alpha\|$ is the spectral norm of the Hessian of the merit function with respect to α (given by the square root of the maximum eigenvalue of $\mathbf{H}_\alpha^T \mathbf{H}_\alpha$). We note that faster algorithms like FISTA (Beck & Teboulle 2009; Asensio Ramos & de la Cruz Rodríguez 2015) can also be used.

Given the simple dependence of $\chi_{\mathbf{q},\alpha}^2$ on α , it can be proven (e.g., Starck et al. 2010) that Eq. (10) can be simplified to finally obtain:

$$\alpha_{i+1} = \text{prox}_{p,\lambda,\mathbf{W}} [\mathbf{S}_{\text{atm}}(\mathbf{q}_{i+1}) - \mathbf{O}] \quad \text{with } \mathbf{q}_{i+1} \text{ fixed.} \quad (11)$$

In other words, the estimation of the systematic effects for a new iteration is very simple and reduces to computing the proximal projection of the residual between the observed Stokes profiles and the current modeled ones. We think that this approach gives a very transparent and intuitive understanding of what the algorithm is doing. We note that the best results have been found applying Eq. (11) every ~ 3 iterations of the LM algorithm.

3.2. The synthesis penalty

When \mathbf{q} is fixed, Eq. (7) becomes again a sparsity-constrained problem for α . In this case, the sparsity penalty $h(\alpha) = \|\alpha\|_p$ is much simpler, but the function $g(\alpha) = \chi_{\mathbf{W}^T}^2(\mathbf{q}, \alpha)$ is more complex because of the presence of the synthesis operator \mathbf{W}^T . We propose to solve the problem using the following first-order iterative scheme:

$$\alpha_{i+1} = \text{prox}_{p,\lambda,\tau} \left[\alpha_i - \tau \nabla_{\alpha} \chi_{\mathbf{W}^T}^2(\mathbf{q}_{i+1}, \alpha_i) \right] \quad \text{with } \mathbf{q}_{i+1} \text{ fixed,} \quad (12)$$

where $\tau < 2/\|\mathbf{H}_\alpha\|^2$, which can be computed from the spectral norm of the transformation matrix \mathbf{W} , and the proximal operator $\text{prox}_{p,\lambda,\tau}$ is described in the following. We point out that a more complex second-order iterative scheme is discussed in the Appendix.

3.3. Computing the proximal operators

The previous iterative schemes rely on the existence of algorithms for the computation of the proximal projection operators $\text{prox}_{p,\lambda,\tau}(\alpha)$ and $\text{prox}_{p,\lambda,\mathbf{W}}(\alpha)$.

3.3.1. Computing $\text{prox}_{p,\lambda,\tau}(\alpha)$

This operator is very simple to compute for typical choices of p (Parikh & Boyd 2014). Useful cases of the regularization term are the ℓ_0 -norm ($p = 0$) or the ℓ_1 -norm ($p = 1$). In the case of the ℓ_0 -norm, the proximal operator reduces to the hard-thresholding operator, which is trivially given by

$$\text{prox}_{p=0,\lambda,\tau}(\alpha) = \begin{cases} \alpha & |\alpha| > \tau\lambda \\ \mathbf{0} & \text{otherwise.} \end{cases} \quad (13)$$

where τ is the step-size defined in §3.1 and λ is the regularization parameter that we introduced in Eq. 5. For the ℓ_1 -norm, it reduces to the soft-thresholding operator, which is given by

$$\text{prox}_{p=1,\lambda,\tau}(\alpha) = \text{sign}(\alpha)(|\alpha| - \tau\lambda)_+, \quad (14)$$

where $(\cdot)_+$ denotes the positive part. Other proximal operators with analytical expressions can be found in Parikh & Boyd (2014).

3.3.2. Computing $\text{prox}_{p,\lambda,\mathbf{W}}(\alpha)$

The solution of Eq. (11) for any \mathbf{W} , either orthogonal or not, is slightly more complicated and requires some elements of proximal calculus (Parikh & Boyd 2014). A general algorithm for the solution of the proximal projection of Eq. (11) has been developed by Fadili & Starck (2009), that we reproduce in Alg. 1 for

Data: \mathbf{W} and α

Result: $\text{prox}_{p,\lambda,\mathbf{W}}(\alpha)$

Initialization: $\mathbf{y}_1 = \alpha$ and suitable step $\tau < 2/\|\mathbf{W}\|^2$;

while not converged do

1. $\mathbf{r} = \alpha - \mathbf{W}\mathbf{y}_i$;
2. $\mathbf{s} = \tau\mathbf{y}_i + \mathbf{W}^T\mathbf{r}$;
3. $\mathbf{y}_{i+1} = \alpha - \tau^{-1}\mathbf{W}[\mathbf{s} - \text{prox}_{p,\lambda,\tau}(\mathbf{s})]$;

end

return \mathbf{y}_i

Algorithm 1: Algorithm for proximal projection, extracted from Fadili & Starck (2009).

Data: Stokes profiles, model atmosphere, transform \mathbf{W} and k .

Result: Regularized solution

Initialization: \mathbf{q}_0 and $\alpha_0 = 0$, first estimation of solution;

while not converged do

1. Compute gradient $\nabla_q \chi_1^2(\mathbf{q}_i, \alpha_i)$ and Hessian matrices \mathbf{H}_q ;
2. Modify Hessians: $\hat{\mathbf{H}}_q = \mathbf{H}_q + \beta \text{diag}(\mathbf{H}_q)$;
3. Update \mathbf{q} : $\mathbf{q}_{i+1} = \mathbf{q}_i - \hat{\mathbf{H}}_q^{-1} \nabla_q \chi_1^2(\mathbf{q}_i, \alpha_i)$;
4. Update α : $\alpha_{i+1} = \text{prox}_{p,\lambda,\mathbf{W}}[\mathbf{S}_{\text{atm}}(\mathbf{q}_{i+1}) - \mathbf{O}]$ using Alg. 1 every k iterations.

end

return \mathbf{q}, α

Algorithm 2: Proximal Levenberg-Marquardt algorithm for analysis penalty.

completeness. We note that the algorithm is just a simple iterative scheme that has been proven to converge to the solution provided the step size $\tau < 2/\|\mathbf{W}\|^2$.

It is interesting to point out that, when \mathbf{W} is an orthogonal transform, Alg. 1 hugely simplifies and the solution to Eq. (11) can be obtained with (Starck et al. 2010):

$$\alpha = \mathbf{W}^T \left[\text{prox}_{p,\lambda,\tau}(\mathbf{W}\alpha) \right]. \quad (15)$$

In other words, the vector α is first transformed, it is then thresholded using the appropriate proximal operator, and finally transformed back to the original domain. If the transformation is unitary, so that $\mathbf{W}^T\mathbf{W} = \mathbf{I}$, the result of the application of Eq. (15) leaves the value of α unchanged for $\lambda = 0$.

Another interesting use of Eq. (15) is that it is equivalent to the first iteration of Alg. 1. We carry out experiments in the following sections to verify if using this simple approximation in the general case of non-orthogonal \mathbf{W} gives good results.

3.4. Selection of λ

As we show in the next section, λ has a strong impact on the sparsity of the final solution. When λ is too small, overfitting clearly appears. On the contrary, if λ is large, the fit is typically of bad quality. Therefore, the selection of λ requires some fine-tuning, but it is possible to have an order of magnitude estimation using very simple arguments. As noted in Eqs. (13) and (14), the thresholding happens for values of the α parameters larger than $\tau\lambda$. Therefore, if we want to avoid values of α smaller than η , then $\lambda \sim \eta/\|\mathbf{W}\|^2$. For the orthogonal unitary transforms, we find that the spectral norm is $\|\mathbf{W}\| = 1$.

3.5. Summary

The full step-by-step algorithms are described in Algs. 2 and 3, together with Alg. 1 for the application of the proximal operator described in step 4 of Alg. 2. We want to clarify to any potential user of this method that the only real difference between current inversion codes for the Stokes parameters and our approach is in point 4 of Alg. 2, together with the necessity to include the systematic effects in the calculation of the gradient and Hessian with respect to the \mathbf{q} variables. This step is very easy to carry out and can be implemented in any existing inversion code with only a few lines of programming.

4. Examples

In this section we demonstrate the capabilities of Algs. 2 and 3 in the inversion of Stokes profiles using several transformation matrices \mathbf{W} and two datasets. For simplicity and for the purpose of clarity, we only focus on Stokes I , for which the systematic effects are usually more important. Throughout this section, we use the ℓ_0 -norm as regularization, so we apply the proximal operator of Eq. (13). The codes used in this paper can be obtained from <https://github.com/aasensio/proxStokesSystematics>.

4.1. Observations

To show examples of application, we choose two spectral regions of special interest that suffer from the problems described in this paper. The first one is the region around 10830 Å, which contains the He I multiplet at 10830 Å and is displayed in the right panel of Fig. 1. This multiplet is used for diagnosing the magnetic properties of chromospheric material. Due to the potentially large Doppler shifts in the chromosphere (e.g., Lagg et al. 2007), it is interesting to apply our approach to this multiplet.

The observations that we analyze have been obtained with the Vacuum Tower Telescope (VTT) on the Observatorio del Teide with the TIP-II instrument (Collados et al. 2007). The profiles have been extracted from a plage region close to a pore. The He I multiplet is synthesized with the help of HAZEL (Asensio Ramos et al. 2008), which gives the $\mathbf{S}_{\text{atm}}(\mathbf{q})$ part of Eq. (1). The spectral lines are characterized by the optical depth on the red component of the multiplet $\Delta\tau$, the Doppler broadening of the line v_{th} and the bulk velocity of the plasma v .

The second region is the well-known region around 6301-6302 Å that contains an Fe I doublet. This region also contains two telluric absorptions. The Stokes profiles, shown in the left panel of Fig. 1, have been obtained from the ground with the Polarimetric Littrow Spectrograph (POLIS; Beck et al. 2005) and belong to the observations of the quiet Sun analyzed by Martínez González et al. (2008).

To fit the profiles, we choose an atmosphere in local thermodynamic equilibrium and we infer the depth stratification of the temperature, velocity along the line-of-sight and microturbulent velocity. For this experiment we fix the number of nodes of the parameterization: 5 nodes for the temperature, 3 for the bulk velocity and 1 for the microturbulent velocity. Like virtually all inversion codes with depth stratification (e.g., Ruiz Cobo & del Toro Iniesta 1992), we place the nodes equispaced in the $\log \tau_c$ axis, with τ_c the continuum optical depth at 5000 Å.

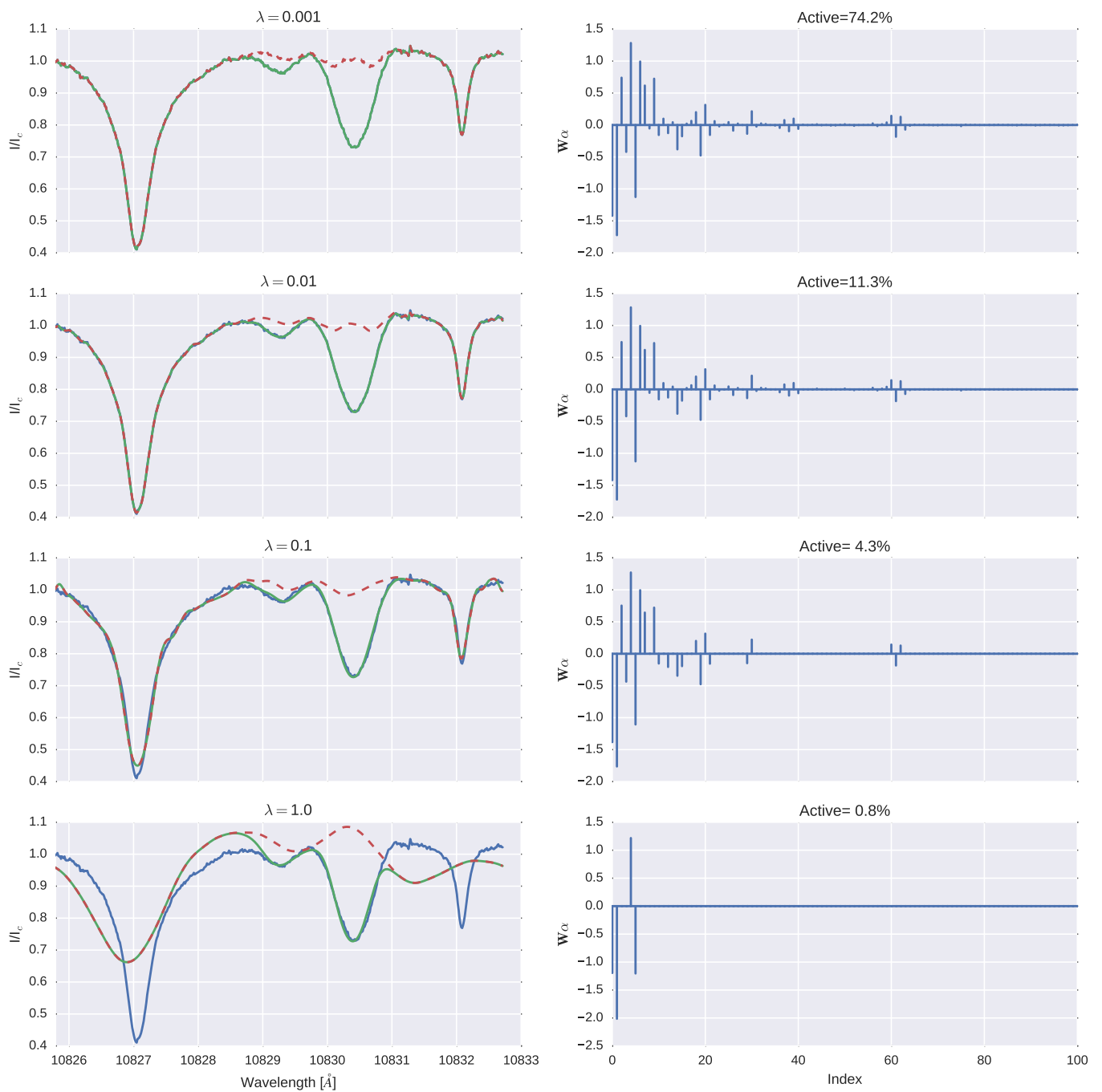


Fig. 2. Left panels: observed (blue) and fitted (green) Stokes I profile for different values of the regularization parameters λ and using an orthogonal wavelet transform as the sparsity-inducing transformation. The dashed red curve shows the inferred systematic effects. The spectral range corresponds to that around the He I multiplet at 10830 Å. Right panels: first 100 active wavelet coefficients of the set of 512 total coefficients. The percentage of active functions is shown in each panel.

4.2. Orthogonal wavelet regularization

The orthogonal wavelet transform (Jensen & la Cour-Harbo 2001) is a very powerful sparsity-inducing transformation in cases in which the signal is smooth. One of the advantages of the orthogonal wavelet transform is that a fast algorithm to compute the direct and inverse transformation exists, without ever computing the transformation matrix \mathbf{W} .

The specific approach for orthogonal transformations is irrelevant because both the analysis and synthesis penalties are equivalent. For convenience, we choose to do this study un-

der the analysis penalty case. We impose the sparsity constraint using the transformation matrix \mathbf{W} associated with the Daubechies-8 orthogonal wavelet and for different values of the regularization parameter λ . The results are shown in Fig. 2. The left panel displays the observed data in blue, the final fit in green (including systematic effects) and the inferred systematic effects in dashed red. The right panel shows the wavelet coefficients of the systematic effects, showing only the first 100 coefficients of the potential 512 coefficients (the wavelength axis contains 512 sampled points). Each panel contains the percentage of ac-

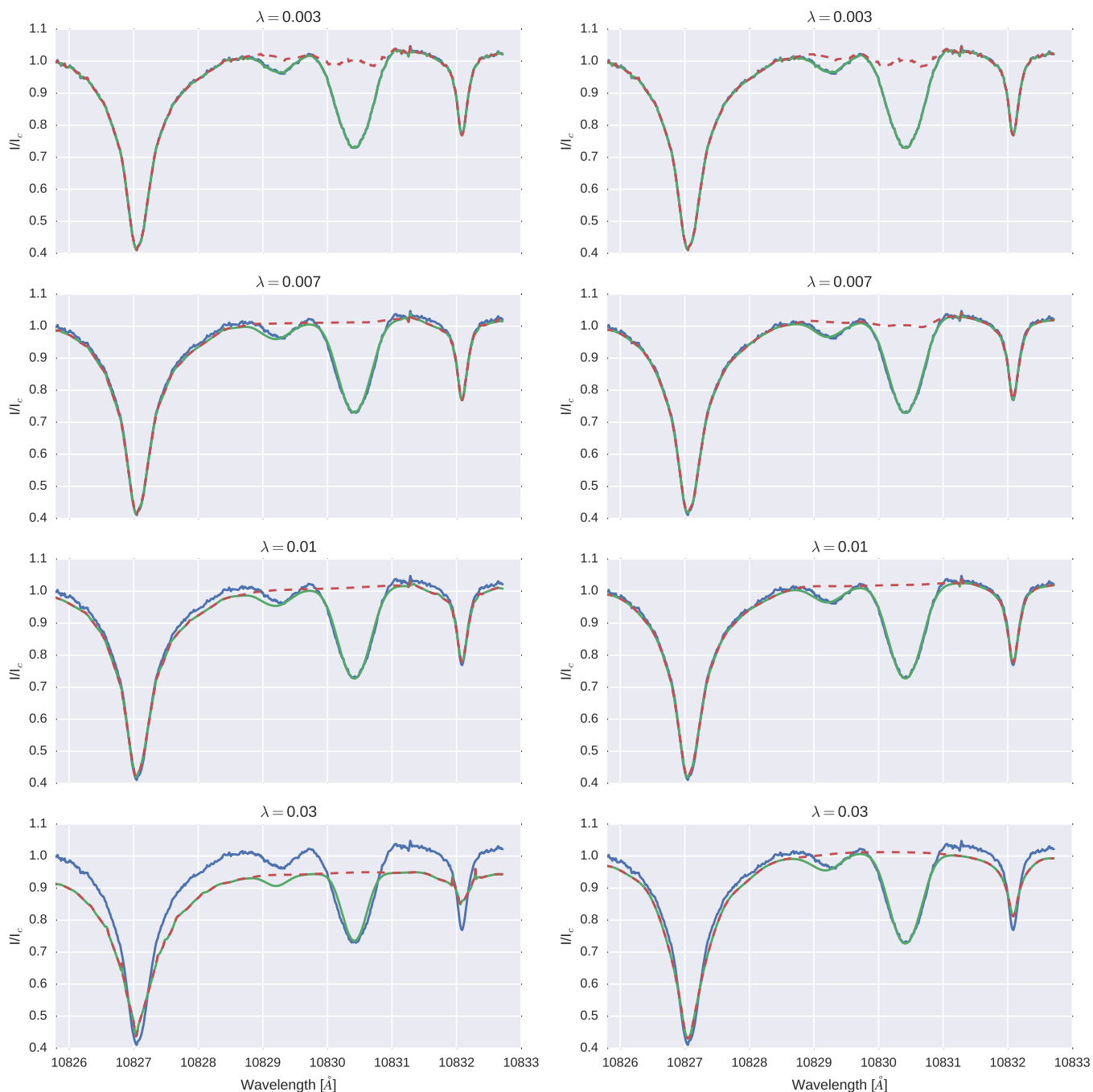


Fig. 3. Observed (blue), fitted (green) and systematic effects (dashed red) obtained using the IUWT in the region around 10830 Å and using the updated version of HAZEL. The left panels correspond to using the full Alg. 1, while the right panel shows the results when using the simplified Eq. (15).

tive (non-zero) wavelet coefficients. Note that the fit quality is strongly affected by the value of the regularization parameters λ . The important point is that it is possible to find values of λ that lead to a good fit of the He I multiplet and simultaneously fit the systematic effects. Of special relevance in this case is the extended wing of the Si I, which sometimes makes it difficult to set a continuum level for the 10830 Å multiplet. Using this approach, the continuum level is automatically obtained from the fit.

When λ is small, a strong overfitting of the data occurs, in which even the noise is absorbed by the systematic effects. For

very large λ , the method cannot fit the observations. For intermediate values of λ , a very nice fit is obtained. The optimal thresholding of the wavelet coefficients is similar to the expected noise level, as pointed out by Starck et al. (2010). Using only 10% of the wavelet coefficients is probably enough to have a fit of the whole spectral region. It is interesting to note that the model that we impose for the He I multiplet is probably not enough for explaining the observations at the noise level. This is the reason why some “extra absorption” is added by the systematic effects to the wings of the red component. If this behavior is undesirable, it is potentially possible to introduce an extra regularization

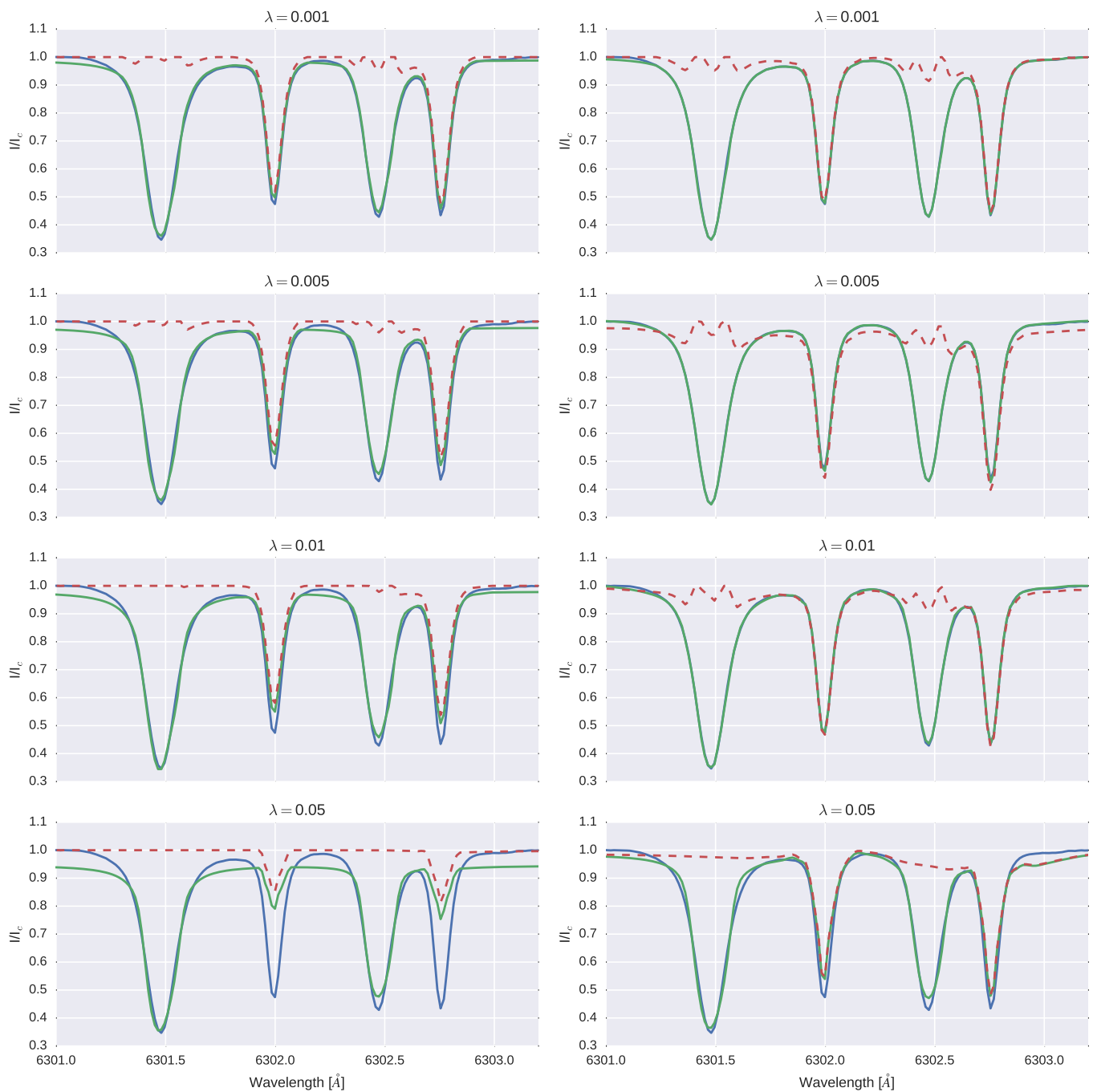


Fig. 4. Observed (blue), fitted (green) and systematic effects (dashed red) obtained using the IUWT in the 6301-6302 Å spectral region and using the inversion code that assumes local thermodynamic equilibrium. The left panels correspond to using the full Alg. 1, while the right panel shows the results when using the simplified Eq. (15).

to avoid them (for instance, an additional ℓ_0 or ℓ_1 regularization for the vector α). However, we demonstrate in the following that a better option is to regularize using different \mathbf{W} transformations.

4.3. Isotropic undecimated wavelet regularization

The isotropic undecimated wavelet transform (IUWT; Starck & Murtagh 1994; Starck et al. 2010) algorithm is a non-orthogonal redundant multiscale transform that is well suited to objects that are more or less isotropic. This transform has found great success for the denoising of astronomical images (e.g., Starck

et al. 2010, and references therein). Recently, we have witnessed examples of applications to one-dimensional spectra (Machado et al. 2013). Given that this is a redundant non-orthogonal transform, the analysis penalty approach is more efficient from a computational point of view.

The IUWT can be efficiently applied using the *à-trous* algorithm, which proceeds as follows. The original data $I(\lambda)$ are filtered, in our case using the B_3 -spline given by the filter $[1, 4, 6, 4, 1]/16$. The filtered data are subtracted from the original ones, obtaining what is commonly known as the *detail*, $w_i(\lambda)$. The filtered data are again iteratively filtered (with scaled fil-

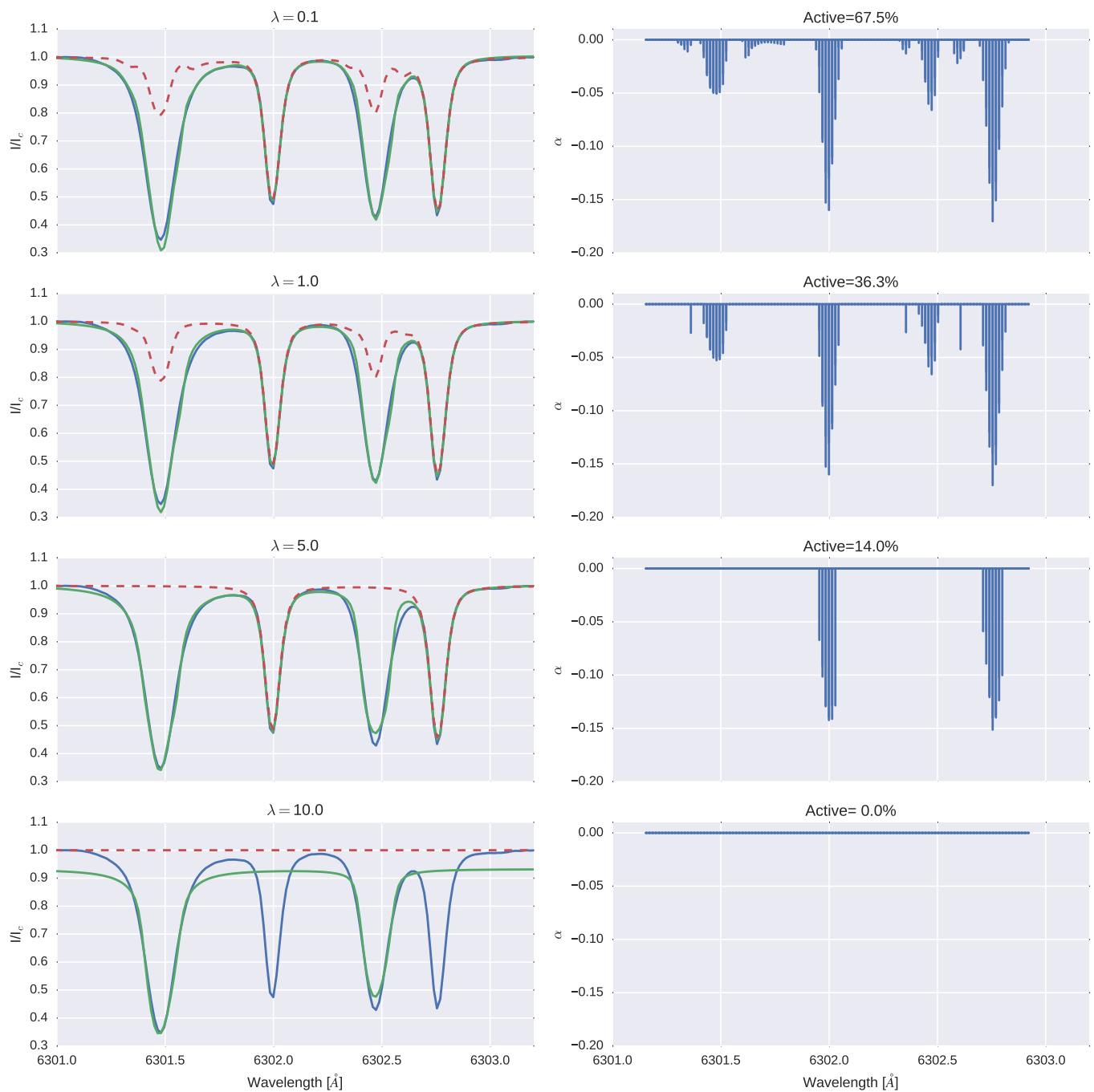


Fig. 5. Observed (blue) and fitted (green) Stokes I profile for different values of the regularization parameters λ and using a dictionary made of Voigt functions centered at every pixel. The dashed red curve shows the inferred systematic effects. The left panels show the results for the Fe I lines, while the right panels show the active functions, with the label indicating the percentage of active functions.

ters) up to a depth d , computing the detail in each scale. The final smoothed signal will be termed $c_d(\lambda)$. At the end, we have a smoothed version of the original signal and a set of *details* at each depth. The size of the IUWT is $d + 1$ times the original data, so the information is really encoded on the correlation among the transformed coefficients. The data are reconstructed from the transformed data simply using:

$$I(\lambda) = c_d(\lambda) + \sum_{i=1}^d w_i(\lambda). \quad (16)$$

The results shown in Fig. 3 for the He I multiplet and Fig. 4 for the Fe I doublet have been obtained using the IUWT up to $d = 6$ and applying the hard thresholding operator to all the details. The left panel shows the results when the full Alg. 1 is used to apply the proximal algorithm, while the right panels give the result when only the first iteration of this algorithm is used, which corresponds to using Eq. (15). The application of Eq. (15) cannot assure convergence to the correct solution to the problem, but we have tested that it does a very good job. This simplifies the application of our proposed algorithm to any existing inversion

Data: Stokes profiles, model atmosphere, transform \mathbf{W} and k .

Result: Regularized solution

Initialization: \mathbf{q}_0 and $\alpha_0 = 0$, first estimation of solution;

while not converged do

1. Compute gradient $\nabla_q \chi_{\mathbf{W}\mathbf{T}}^2(\mathbf{q}_i, \alpha_i)$ and Hessian matrices \mathbf{H}_q ;
2. Modify Hessians: $\hat{\mathbf{H}}_q = \mathbf{H}_q + \beta \text{diag}(\mathbf{H}_q)$;
3. Update \mathbf{q} : $\mathbf{q}_{i+1} = \mathbf{q}_i - \hat{\mathbf{H}}_q^{-1} \nabla_q \chi_{\mathbf{W}\mathbf{T}}^2(\mathbf{q}_i, \alpha_i)$;
4. Update α : $\alpha_{i+1} = \text{prox}_{p,\lambda,\tau} [\alpha_i - \tau \nabla_\alpha \chi_{\mathbf{W}\mathbf{T}}^2(\mathbf{q}_{i+1}, \alpha_i)]$;

end

return \mathbf{q}, α

Algorithm 3: Proximal Levenberg-Marquardt algorithm for synthesis penalty.

code because Eq. (15) can be implemented in only one or a few lines of code.

When the value of λ is small, we witness again the overfitting, which also includes the addition of some broadening of the red component of the He I. When λ is large, the fit is of low quality. In the intermediate range close to the expected noise standard deviation, we find an excellent fit of the whole profile, with a flat contribution exactly where the He I multiplet is located.

It is interesting to note that we have empirically found that applying Eq. (15) instead of solving the full problem via Alg. 1 gives better and more robust results (see Figs. 3 and 4). The reason has to be found on the fact that we are solving the optimization problem of Eqs. (5) or (7) by separating it into two simpler problems via an alternating optimization method. It is a general characteristic of these methods that they work better in practice if none of the two problems is solved with full precision at each iteration, but only approximately. If any of the two problems is solved with precision in any iteration, one can produce some amount of overfitting that is very difficult to compensate for in later iterations.

4.4. Voigt functions

The final example uses another non-orthogonal and redundant transformation, in this case not of general applicability, but tailored to explain the systematic effects. The Hermite functions described by del Toro Iniesta & López Ariste (2003) is a good option, but we prefer to utilize a basis set made of Voigt functions centered at every sampled wavelength point:

$$\phi_i(\lambda) = H\left(\frac{\lambda - \lambda_i}{\Delta}, a\right). \quad (17)$$

Even though the basis is non-orthogonal, it is much easier in this case to work in the synthesis prior approach, because the results are much more transparent. The reason is that we directly impose the sparsity constraint on the coefficients associated with all the Voigt functions.

In this case, we focus on the 6301-6302 Å spectral region. The systematic effects are modeled with Voigt functions placed at every sampled wavelength between 6301.15 and 6302.93 Å, which includes both Fe I lines and both telluric contaminations. The damping constant is fixed to $a = 0.8$, which gives line wings similar to those observed in the telluric lines. To boost sparsity, we consider two different widths, $\Delta = 14.8, 29.6$ mÅ, although more fits and damping parameters can be easily considered with ease.

The results are displayed in Fig. 5 for different values of λ . The left panel shows the observations and the fit, together with the inferred systematic effects. The right panel shows the active Voigt functions. When λ is too small, a very good fitting is found, but we can see that the optimization induces corrections on the spectral lines of interest. This is, in principle, undesired, although it is clearly stating that the model proposed for the spectral lines cannot fit them with enough precision. When λ is large, the fit of the systematic effects is bad, which negatively impacts the fit of the spectral lines of interest. For intermediate values of the regularization parameter, we find an acceptable fit, where only the telluric absorption lines are fitted by the systematic effects with a very sparse solution.

5. Conclusions

In the present study we have developed a new method that allows to deal with systematic effects in data inversions. These systematic effects can include a variety of calibration defects, spectral lines from the Earth's atmosphere or spectral features that are present in the observations that our model atmosphere cannot reproduce. Our method builds upon the assumption that these systematic effects are not random noise and therefore they have an inherent *level of sparsity* in a suitable basis set.

We have shown that the assumption of sparsity induces a very powerful regularization because the resulting cross-talk between the inversion model and the systematic effects can be made very low. To do so, we have introduced a regularization parameter λ that must be adjusted according to the needs of each problem based on experience. However, we argue that this step is not very different from selecting the weights of the observations in current implementations of inversions codes and a rough estimate can be obtained *a-priori*.

Although the mathematical characterization of the algorithm can appear a bit convoluted and depends on recent advances on the optimization of non-smooth functions, a few extra lines of code should suffice to make it work with current inversion codes. Our experience with the SIR and Hazel codes has positively confirmed it. When these systematic effects are not corrected, inversion codes usually try to overcompensate their effect by converging the parameters of the model to a wrong solution. Our method minimizes the impact of such effects in the convergence of the solution when an adequate value of the regularization parameter is selected.

Our method has a few interesting advantages over the down-weighting technique for dealing with systematic effects. Arguably the most important one concerns the assumptions imposed on the generative model. Using the χ^2 merit function requires that the uncertainty of the residual between the observations and the model is Gaussian with zero mean and a certain variance. This is not true unless one is able to *model all* expected signals. Only if everything is modeled (to a certain level, of course), one is sure that the results can be interpreted appropriately (for instance, error bars). A second advantage concerns the reduction in the subjectivity on the election of parameters. One only needs to choose the value of λ and the method automatically adapts the solution to the systematic effects.

Appendix A: Second-order iterative scheme in the synthesis prior

It is possible to use a second-order iterative scheme that would improve over Eq. (12) when using the synthesis prior approach.

Data: \mathbf{H}_α and α

Result: $\text{prox}_h^H(\alpha)$

Initialization: $t_0 = 1$, $\mathbf{y}_1 = \alpha$ and step $\tau < 2/\|\mathbf{H}_\alpha\|^2$;

while not converged do

1. Update values: $\mathbf{y}'_{i+1} = \mathbf{y}_i - \tau \mathbf{H}_\alpha(\mathbf{y}_i - \alpha)$;
2. Apply projection: $\alpha_{i+1} = \text{prox}_{p,\lambda,\tau}(\mathbf{y}'_{i+1})$;
3. Update weight: $t_{i+1} = \frac{1 + \sqrt{1 + 4t_i^2}}{2}$;
4. Update solution: $\mathbf{y}_{i+1} = \mathbf{y}_i + \left(\frac{t_i - 1}{t_{i+1}}\right)(\mathbf{y}'_{i+1} - \mathbf{y}_i)$;

end

return \mathbf{y}_i

Algorithm 4: FISTA algorithm for scaled proximal projection.

Instead of a simple step τ , one uses the full Hessian, so that the iterative scheme is updated to read (Lee et al. 2012):

$$\alpha_{i+1} = \text{prox}_{p,\lambda}^{H_\alpha} \left[\alpha_i - \mathbf{H}_\alpha^{-1} \nabla_{\alpha} \chi_{\text{WT}}^2(\mathbf{q}_{i+1}, \alpha_i) \right] \quad \text{with } \mathbf{q}_{i+1} \text{ fixed.} \quad (\text{A.1})$$

The main obstacle is the computation of the so-called scaled proximal operator $\text{prox}_{p,\lambda}^{H_\alpha}(\alpha)$. It can be demonstrated that this proximal operator can be efficiently computed using the accelerated FISTA iteration (Beck & Teboulle 2009) that is displayed in Alg. 4.

Acknowledgements. Financial support by the Spanish Ministry of Economy and Competitiveness through projects AYA2014-60476-P, AYA2014-60833-P and Consolider-Ingenio 2010 CSD2009-00038 are gratefully acknowledged. JdlCR is supported by grants from the Swedish Research Council (Vetenskapsrådet) and the Swedish National Space Board. AAR also acknowledges financial support through the Ramón y Cajal fellowship. This research has made use of NASA's Astrophysics Data System Bibliographic Services. This article is based on observations taken with the VTT telescope operated on the island of Tenerife by the Kiepenheuer-Institut für Sonnenphysik in the Spanish Observatorio del Teide of the Instituto de Astrofísica de Canarias (IAC). We acknowledge the community effort devoted to the development of the following open-source Python packages that were used in this work: `numpy`, `matplotlib`, `scipy`, `seaborn` and `PyWavelets`.

References

- Asensio Ramos, A. 2009, ApJ, 701, 1032
 Asensio Ramos, A. & de la Cruz Rodríguez, J. 2015, A&A, 577, A140
 Asensio Ramos, A., Manso Sainz, R., Martínez González, M. J., et al. 2012, ApJ, 748, 83
 Asensio Ramos, A., Martínez González, M. J., & Rubiño Martín, J. A. 2007, A&A, 476, 959
 Asensio Ramos, A., Trujillo Bueno, J., & Landi Degl'Innocenti, E. 2008, ApJ, 683, 542
 Auer, L. H., House, L. L., & Heasley, J. N. 1977, Sol. Phys., 55, 47
 Beck, A. & Teboulle, M. 2009, SIAM J. Img. Sci., 2, 183
 Beck, C., Schmidt, W., Kentischer, T., & Elmore, D. 2005, A&A, 437, 1159
 Borrero, J. M., Tomczyk, S., Kubo, M., et al. 2010, Sol. Phys., 35
 Borrero, J. M., Tomczyk, S., Norton, A., et al. 2007, Sol. Phys., 240, 177
 Candès, E., Romberg, J., & Tao, T. 2006, Comm. Pure Appl. Math., 59, 1207
 Collados, M., Lagg, A., Díaz García, J. J., et al. 2007, in Astronomical Society of the Pacific Conference Series, Vol. 368, The Physics of Chromospheric Plasmas, ed. P. Heinzel, I. Dorotovič, & R. J. Rutten, 611
 del Toro Iniesta, J. C. & López Ariste, A. 2003, A&A, 412, 875
 Donoho, D. 2006, IEEE Trans. on Information Theory, 52, 1289
 Elad, M., Milanfar, P., & Rubinstein, R. 2007, Inverse Problems, 23, 947
 Fadili, M. J. & Starck, J.-L. 2009, in Proc. IEEE International Conference on Image Processing
 Harvey, J., Livingston, W., & Slaughter, C. 1972, in Line Formation in the Presence of Magnetic Fields, 227–+
 Jensen, A. & la Cour-Harbo, A. 2001, Ripples in Mathematics: The Discrete Wavelet Transform (Springer Verlag)
 Lagg, A., Woch, J., Solanki, S. K., & Krupp, N. 2007, A&A, 462, 1147
 Landi Degl'Innocenti, E. & Landi Degl'Innocenti, M. 1977, A&A, 56, 111

- Landi Degl'Innocenti, E. & Landolfi, M. 2004, Polarization in Spectral Lines (Kluwer Academic Publishers)
 Lee, J. D., Sun, Y., & Saunders, M. A. 2012, SIAM Journal on Optimization, 24, 3
 Levenberg, K. 1944, Q. J. Math., 2, 164
 Lites, B., Casini, R., Garcia, J., & Socas-Navarro, H. 2007, Mem. Soc. Astron. Ital., 78, 148
 Machado, D. P., Leonard, A., Starck, J.-L., Abdalla, F. B., & Jouvel, S. 2013, A&A, 560, A83
 Marquardt, D. 1963, SIAM J. Appl. Math., 11, 431
 Martínez González, M. J., Collados, M., Ruiz Cobo, B., & Beck, C. 2008, A&A, 477, 953
 Orozco Suárez, D., Bellot Rubio, L. R., del Toro Iniesta, J. C., et al. 2007, ApJL, 670, L61
 Parikh, N. & Boyd, S. 2014, Foundations and Trends in Optimization, 1
 Ruiz Cobo, B. & Asensio Ramos, A. 2013, A&A, 549, L4
 Ruiz Cobo, B. & del Toro Iniesta, J. C. 1992, ApJ, 398, 375
 Ruiz Cobo, B. & del Toro Iniesta, J. C. 1994, A&A, 283, 129
 Sanchez Almeida, J. 1992, Sol. Phys., 137, 1
 Skumanich, A. & Lites, B. W. 1987, ApJ, 322, 473
 Socas-Navarro, H., de la Cruz Rodríguez, J., Asensio Ramos, A., Trujillo Bueno, J., & Ruiz Cobo, B. 2014, ArXiv e-prints
 Socas-Navarro, H., Trujillo Bueno, J., & Ruiz Cobo, B. 2000, ApJ, 530, 977
 Starck, J.-L. & Murtagh, F. 1994, A&A, 288, 342
 Starck, J.-L., Murtagh, F., & Fadili, J. M. 2010, Sparse image and signal processing (Cambridge: Cambridge University Press)
 van Noort, M. 2012, A&A, 548, A5